



Publication Year	2018
Acceptance in OA	2020-10-21T13:08:53Z
Title	Calibration of AGILE-GRID with On-ground Data and Monte Carlo Simulations
Authors	Cattaneo, P. W., Rappoldi, A., ARGAN, ANDREA, Barbiellini, G., Boffelli, F., BULGARELLI, ANDREA, Buonomo, B., CARDILLO, MARTINA, Chen, A. W., Cocco, V., Colafrancesco, S., D'AMMANDO, FILIPPO, Donnarumma, I., Ferrari, A., FIORETTI, VALENTINA, Foggetta, L., Froyland, T., FUSCHINO, FABIO, Galli, M., GIANOTTI, FULVIO, GIULIANI, ANDREA, Longo, F., LUCARELLI, Fabrizio, Marisaldi, M., Mazzitelli, G., Morselli, A., Paoletti, F., Parmigiani, N., PELLIZZONI, ALBERTO PAOLO, PIANO, Giovanni, PILIA, Maura, PITTORI, Carlotta, Prest, M., Pucella, G., Quintieri, L., Sabatini, S., TAVANI, MARCO, TRIFOGLIO, MASSIMO, TROIS, ALESSIO, Valente, P., Vallazza, E., VERCELLONE, STEFANO, VERRECCHIA, Francesco, Zambra, A.
Publisher's version (DOI)	10.3847/1538-4357/aac888
Handle	http://hdl.handle.net/20.500.12386/27904
Journal	THE ASTROPHYSICAL JOURNAL
Volume	861

Calibration of AGILE-GRID with on-ground data and Monte Carlo simulations

P.W. CATTANEO,¹ A. RAPPOLDI,¹ A. ARGAN,² G. BARBIELLINI,³ F. BOFFELLI,¹ A. BULGARELLI,⁴ B. BUONOMO,⁵ M. CARDILLO,² A.W. CHEN,⁶ V. COCCO,² S. COLAFRANCESCO,^{6,7} F. D'AMMANDO,⁸ I. DONNARUMMA,^{2,9} A. FERRARI,¹⁰ V. FIORETTI,⁴ L. FOGGETTA,⁵ T. FROYSLAND,^{11,10} F. FUSCHINO,⁴ M. GALLI,¹² F. GIANOTTI,⁴ A. GIULIANI,¹³ F. LONGO,^{14,3} F. LUCARELLI,^{15,7} M. MARISALDI,^{16,4} G. MAZZITELLI,⁵ A. MORSELLI,¹⁷ F. PAOLETTI,^{18,2} N. PARMIGIANI,⁴ A. PELLIZZONI,¹⁹ G. PIANO,^{2,10} M. PILIA,¹⁹ C. PITTORI,^{15,7} M. PREST,²⁰ G. PUCELLA,²¹ L. QUINTIERI,⁵ S. SABATINI,² M. TAVANI,^{2,11} M. TRIFOGLIO,⁴ A. TROIS,¹⁹ P. VALENTE,²² E. VALLAZZA,³ S. VERCELLONE,²³ F. VERRECCHIA,^{15,7} AND A. ZAMBRA¹³

¹*INFN-Pavia, Via A. Bassi 6, I-27100 Pavia, Italy*

²*INAF/IAPS-Roma, via del Fosso del Cavaliere 100, I-00133 Roma, Italy*

³*INFN-Trieste, Via A. Valerio 2, I-34127 Trieste, Italy*

⁴*INAF/IASF-Bologna, Via P. Gobetti 101, I-40129 Bologna, Italy*

⁵*INFN Lab. Naz. di Frascati, Via E. Fermi, 40, I-00044 Frascati(Roma), Italy*

⁶*School of Physics, Wits University, Johannesburg, South Africa*

⁷*INAF-Osservatorio Astronomico di Roma, Via Frascati 33, I-00078 Monte Porzio Catone (Roma), Italy*

⁸*INAF-IRA Bologna, Via Gobetti 101, I-40129 Bologna, Italy*

⁹*Agenzia Spaziale Italiana (ASI), Via del Politecnico snc, I-00133 Roma, Italy*

¹⁰*CIFS, c/o Dip. Fisica, Univ. di Torino, Via P. Giuria 1, I-10125 Torino, Italy*

¹¹*Dip. di Fisica, Univ. Tor Vergata, Via della Ricerca Scientifica 1, I-00133 Roma, Italy*

¹²*ENEA-Bologna, Via Martiri di Monte Sole 4, I-40129 Bologna, Italy*

¹³*INAF/IASF-Milano, Via E. Bassini 15, I-20133 Milano, Italy*

¹⁴*Dip. Fisica, Univ. di Trieste, Via A. Valerio 2, I-34127 Trieste, Italy*

¹⁵*ASI Space Science Data Center (SSDC), Via del Politecnico snc, I-00133 Roma, Italy*

¹⁶*Birkeland Centre for Space Science, Department of Physics and Technology, University of Bergen, Norway*

¹⁷*INFN-Roma Tor Vergata, Via della Ricerca Scientifica 1, I-00133 Roma, Italy*

¹⁸*East Windsor RSD, 25a Leshin Lane, Hightstown, NJ 08520, USA*

¹⁹*INAF-Osservatorio Astronomico di Cagliari, Via della Scienza 5, I-09047 Selargius (CA), Italy*

²⁰*Univ. dell'Insubria, Via Valleggio 11, I-22100 Como, Italy*

²¹*ENEA-Frascati, Via E. Fermi, 45, I-00044 Frascati (Roma), Italy*

²²*INFN-Roma La Sapienza, Piazzale A. Moro 2, I-00185 Roma, Italy*

²³*INAF-Osservatorio Astronomico di Brera, Via E. Bianchi 46, I-23807 Merate(LC), Italy*

(Dated: May 29, 2018)

Submitted to ApJ

ABSTRACT

AGILE is a mission of the Italian Space Agency (ASI) Scientific Program dedicated to γ -ray astrophysics, operating in a low Earth orbit since April 23, 2007. It is designed to be a very light and compact instrument, capable of simultaneously detecting and imaging photons in the 18 keV to 60 keV X-ray energy band and in the 30 MeV–50 GeV γ -ray energy with a good angular resolution ($\approx 1^\circ @ 1$ GeV). The core of the instrument is the Silicon Tracker complemented with a CsI calorimeter and a AntiCoincidence system forming the Gamma Ray Imaging Detector (GRID). Before launch, the GRID needed on-ground calibration with a tagged γ -ray beam to estimate its performance and validate the Monte Carlo simulation. The GRID was calibrated using a tagged γ -ray beam with energy up to 500 MeV at the Beam Test Facilities at the INFN Laboratori Nazionali di Frascati. These data are used to validate a GEANT3 based simulation by comparing the data and the Monte Carlo simulation by measuring the angular and energy resolutions. The GRID angular and energy resolutions

obtained using the beam agree well with the Monte Carlo simulation. Therefore the simulation can be used to simulate the same performance on-flight with high reliability.

Keywords: Electron and positron beam – Photon beam – Position-sensitive detectors – Bremsstrahlung

1. INTRODUCTION

AGILE (Astro-rivelatore Gamma a Immagini LEggero) is a Small Scientific Mission of the Italian Space Agency (ASI) dedicated to high-energy γ -ray astrophysics (Tavani et al. 2008, 2009), composed of a Gamma Ray Imager Detector (GRID) sensitive in the energy range 30 MeV–50 GeV (Barbiellini et al. 2002; Prest et al. 2003), a hard X-ray imager (Super-AGILE) sensitive in the energy range 18 keV to 60 keV (Feroci et al. 2007) and a Mini-Calorimeter (MCAL) sensitive to γ -rays and charged particles in the energy range 350 keV to 100 MeV (Labanti et al. 2009). At the core of the GRID, there is a Silicon Tracker (ST) for detection of γ -rays through pair production.

A correct interpretation of the GRID measurements relies on a precise calibration of the instrument. This is based on a combination of on-ground calibration, Monte Carlo (MC) simulation and on-flight calibration. The goal of the present paper is to validate the MC simulation of the GRID by comparing the data and the MC simulation of the on-ground calibration with a γ -ray tagged beam with energy up to 500 MeV. For in-flight calibration see Chen 2012; Chen et al. 2013.

2. THE AGILE INSTRUMENT

The AGILE scientific payload (sketched in its main components in Fig. 1) consists of three instruments with independent detection capability.

The Gamma-Ray Imaging Detector (GRID) consists of a Silicon-Tungsten converter-tracker (ST) with excellent spatial resolution and good timing capability, a shallow ($1.5 X_0$ on-axis) Caesium Iodide MCAL and an AntiCoincidence system (AC) made of plastic slab (Perotti et al. 2006). It has an unprecedented large field of view (FOV) covering ≈ 2.5 sr, almost 1/4 of the entire sky, in the energy range 30 MeV–50 GeV.

The hard X-ray imager (Super-AGILE) is a coded-masked system made of a silicon detector plane and tungsten mask above it designed to image photons over a large FOV (≈ 1 sr).

MCAL operates also stand alone in “burst mode” covering the range 350 keV to 100 MeV to detect GRB and other γ -ray transients.

2.1. The Silicon Tracker

The core of the GRID is the ST with the task of converting the incoming γ -rays and measuring the trajectories of the resulting $e^+ - e^-$ pair (Prest et al. 2003; Barbiellini et al. 2002). The γ -rays convert in the W (Si) layers in $e^+ - e^-$ pairs, which are subsequently detected by the silicon microstrip detectors.

The ST consists of 12 trays with distance between middle-planes equal to 1.9 cm. The first 10 trays consists of pairs of single sided Si microstrip planes with strips orthogonal to each other to provide 3D points followed by a W converter layer 245 μm thick (corresponding to $0.01(\text{Si})+0.07(\text{W}) X_0$). The last two trays have no W converter layer since the ST trigger requires at least three Si planes to be activated.

The base detector unit is a tile of area $9.5 \times 9.5 \text{ cm}^2$, thickness 410 μm and strip pitch 121 μm . Four tiles are bonded together to create a ‘ladder’ with 38.0 cm long strip. Each plane of the ST consists of four ladders. The readout pitch is 242 μm .

The ST analogue read-out measures the energy deposited on every second strip; that is ‘readout’ and ‘floating’ strips alternate. This configuration enables to obtain a good compromise between power consumption and position resolution, the latter being $\sim 45 \mu\text{m}$ for perpendicular tracks (Barbiellini et al. 2002).

Each ladder is readout by three TAA1 ASICs, each operating 128 channels at low noise, low power configuration ($< 400 \mu\text{W}/\text{channel}$), self-triggering capability and analogue readout. The total number of readout channels is 36864.

2.2. The GRID simulation

The GRID is simulated using the GEANT 3.21 package (Brun et al. 1993). This package provides for a detailed simulation of the materials and describes with high precision the passage of particles through matter including the production of secondary particles. It provides the user with the possibility of describing the response of the active



Figure 1. Sketch of the AGILE payload, not in scale. The main components are shown: the plastic scintillator Anticoincidence, the Silicon-tungsten tracker, the CsI bars MiniCalorimeter, the hard X-ray imager Super-Agile based on a silicon detector plane and a tungsten mask.

sections of the detector. The GRID detector simulation used in the test beam configuration is used also to simulate the configuration with the detector mounted on the spacecraft.

In a microstrip detector with floating strips a critical aspect of the simulation is the sharing of the charge collected on the strips to the readout channels (Cattaneo 1990). These sharing coefficients are estimated by using test beam data to reproduce the observations (Barbiellini et al. 2002).

The Cartesian coordinate system employed in the following has the origin in the centre of the AC plane on the top, the x and y axis parallel to the orthogonal strips of the ST and the z axis pointing in the direction of MCAL. In the following the corresponding spherical coordinate system defined by the polar angle Θ and azimuthal angle Φ will be extensively used.

2.3. Reconstruction filter

The reconstruction filter processes the reconstructed hits in the ST layers with the goal of providing a full description of the events. The reconstruction filter has several, sometimes conflicting, goals: reconstructing tracks, estimating their directions and energies, combining them to identify γ -ray, rejecting background hits from noise and charged particle escaping the AC veto and providing an estimation of the probability that the measured tracks originate by a pair converted γ -ray. The filter used in this analysis, FM3.119 (Bulgarelli et al. 2010; Chen et al. 2011), is the result of an optimisation between those requirements and has been used in all AGILE scientific analyses.

2.3.1. Direction reconstruction

The reconstruction of the γ -ray direction, defined by the polar angle Θ and azimuthal angle Φ with respect to the AGILE coordinate system, is based on the process of pair production and is obtained from the identification and the analysis of the $e^+ - e^-$ tracks stemming from a common vertex. At each tray the microstrips on the silicon layers measure separately the coordinates x and y of the hits. The first step of the event analysis requires to find the two tracks among the possible associations of the hits detected by the ST layers.

The second step consists in a linear fit of the hits associated to each track. This task is complicated by the electrons moving along not straight line trajectory because of the multiple scattering. These steps are performed separately for the hits corresponding to the x and y coordinates producing four tracks, two for each projection. The direction in three dimension is obtained associating correctly the two projections of each track (Pittori & Tavani 2002).

In order to fit the tracks, a Kalman filter smooth algorithm (Kalman 1960; Früwirth 1987) has been developed (Giuliani et al. 2006). This technique progressively updates the track candidate information during the track finding process, predicting as precisely as possible the next hit to be found along a trajectory. This capability is used to merge into an unique recursive algorithm the track-finding procedure and the fitting of the tracks parameters. It is therefore possible to associate at each fitted track a total χ^2 given by the sum of the χ^2 of each plane of the ST. If the combination of the ST hits gives rise to more than two possible tracks, the χ^2 is used to choose the best pair of reconstructed tracks corresponding to the $e^+ - e^-$ pair originating from the γ -ray conversion vertex.

2.3.2. Energy Measurement

The track reconstruction algorithm is based on a special implementation of the Kalman filter that estimates the energy of the single tracks on the basis of the measurement of the multiple scattering between adjacent planes.

A quantitative estimation of the single track energy resolution can be obtained considering the Gaussian approximation of the standard deviation of the distribution of the 3D multiple scattering angle (p is the particle momentum, β the speed, t/X_0 the thickness of the material expressed in term of radiation length) and the ultrarelativistic approximation ($\beta = c$ and $pc = E$)

$$\sigma_{\text{MS}}(\theta) = \frac{19.2 \text{ MeV}}{c\beta p} \sqrt{\frac{t}{X_0}} \sim \frac{19.2 \text{ MeV}}{cE} \sqrt{\frac{t}{X_0}}. \quad (1)$$

Therefore to estimate the error on energy measurement we can write

$$\begin{aligned} \Delta(\sigma_{\text{MS}}) &= \frac{\Delta(E)}{E} \frac{19.2 \text{ MeV}}{cE} \sqrt{\frac{t}{X_0}} \\ \frac{\Delta(E)}{E} &= \frac{\Delta(\sigma_{\text{MS}})}{\sigma_{\text{MS}}} \end{aligned} \quad (2)$$

The trajectory of a charged particle subject to multiple scattering crossing N measurement planes is a broken line consisting of $N - 1$ segments that define $N_{\text{MS}} = N - 2$ scattering angles. The particle direction projected on one coordinate between the planes k and $k + 1$ at a distance L is given by $(x_{k+1} - x_k)/L$; this variable has an associated measurement error due to the position error $\sigma(x_k)$. If the measurement of the particle direction between measurement

planes is dominated by the change of direction due to multiple scattering (and not by the position measurement error), it provides N_{MS} sampling of the multiple scattering distribution, assuming that the particle energy is constant throughout the tracking. The error associated to the measurement of the standard deviation of the Gaussian distribution in Eq.1 is

$$\Delta(\sigma_{\text{MS}}) = \frac{1}{\sqrt{2N_{\text{MS}}}}\sigma_{\text{MS}}$$

From Eq.2 we obtain

$$\Delta(\log E) = \frac{\Delta(E)}{E} = \frac{\Delta(\sigma_{\text{MS}})}{\sigma_{\text{MS}}} = \frac{1}{\sqrt{2N_{\text{MS}}}}, \quad (3)$$

hence the relative error is independent from the energy and from the thickness of scattering material and therefore from the angle relative to the planes and depends only on the number of hits. In average, having 12 planes, the maximum value for N_{MS} is 10. The average value is half this value ~ 5 . Therefore we expect $\Delta(\log E) \sim 1/\sqrt{2 \times 5} \sim 0.316$.

The high-energy limit of this approach is reached when the size of the deviation from the extrapolated trajectory due to multiple scattering is comparable to the error in position measurement in the measurement plane. From Barbiellini et al. 2002 the measurement error of the single coordinate is $\sigma_x \sim 45 \mu\text{m}$ and, therefore, on the 2D distance in the tracking plane $\sigma_{xy} \sqrt{2} \times \sim 45 \mu\text{m} \sim 64 \mu\text{m}$, while $L=1.9 \text{ cm}$. Hence the limit on the capability of measuring the direction of a track segment, which has two vertices, is $\sigma_{xy}/L \sim 0.0064\sqrt{2}/1.9 \sim 4.8 \times 10^{-3} \text{ rad}$. Recalling that the thickness of a tray is $0.08 X_0$ and that the angular deviation due to multiple scattering is measured from the different between the directions of the track segments, from Eq.1 the particle energy for which the multiple scattering angle is equal to the direction error due to the finite position resolution of the planes is $\sim 0.8 \text{ GeV}$. Therefore in the energy range available in this test the assumption that the multiple scattering contribution dominates over measurement errors is always true.

2.3.3. Event classification

On the basis of the reconstruction results, each event is classified by the filter as a likely γ -ray (G), limbo (L), a particle (P) or a single-track event (S). Limbo events look like G events but not exactly, for example there are additional hits. In practice, all scientific analyses other than pulsar timing and γ -ray bursts have used only G events. Therefore we concentrate on G events in the following.

3. THE GAMMA-RAY CALIBRATIONS

3.1. Calibration goals

The goal of the calibration is to estimate the instrument response functions by means of exposure to controlled γ -ray beams. The ideal calibration beam provides a flux of γ -rays, monochromatic in energy and arriving as a planar wave uniformly distributed on the instrument surface, with properties known to an accuracy better than the resolving power of the instrument.

The figures of merit to be evaluated and compared are the Energy Dispersion Probability (EDP), the Point Spread Function (PSF) and the effective Area (A_{eff}): all of them depend on the incoming γ -ray energy E_γ and direction (Θ, Φ) .

The EDP is the energy response of the GRID detector to a monochromatic planar wave with energy E_γ and direction (Θ, Φ) . It is a function of E_γ and of (Θ, Φ) , defined as

$$EDP(E_\gamma, \Theta, \Phi) = \frac{1}{N(E_\gamma, \Theta, \Phi)} \frac{dN(E_\gamma, \Theta, \Phi)}{dE_{\text{GRID}}}. \quad (4)$$

where E_{GRID} is the energy measured by the GRID.

The PSF is the response in the angular domain of the GRID detector to a planar wave. If γ -rays impinge uniformly on the GRID with fixed direction (Θ, Φ) , the detector measures for each γ -ray a direction (Θ', Φ') . Assuming this function to be azimuthally symmetric, and defining the three-dimensional angular distance θ between the true and measured directions¹, it is defined as

$$PSF(\theta, E_\gamma, \Theta, \Phi) d\theta = 2\pi \sin(\theta) P(\theta, E_\gamma, \Theta, \Phi) d\theta \quad (5)$$

¹ $\cos(\theta)$ is the scalar product of the versors identified by (Θ, Φ) and (Θ', Φ')

where $P(\theta, E_\gamma, \Theta, \Phi)$ is the probability distribution per steradian of measuring an incoming γ -ray at a given angular distance θ from its true direction (Sabatini et al. 2015).

The A_{eff} is a function of E_γ and of (Θ, Φ) , it is defined as

$$A_{\text{eff}}(E_\gamma, \Theta, \Phi) = \int_A \epsilon(E_\gamma, \Theta, \Phi, \bar{x}) da \quad (6)$$

where the integral over the two-dimensional coordinate variables covers the detector area A intercepted by the incoming γ -ray direction and $\epsilon(E_\gamma, \Theta, \Phi, \bar{x})$ is the detection efficiency dependent on the energy and direction of the incoming γ -ray and on the position on the detector.

The GRID was calibrated at the INFN Laboratory of Frascati (LNF) in the period 2-20 November 2005, thanks to a scientific collaboration between AGILE Team and INFN-LNF.

3.2. Calibration strategy

The goal of the GRID calibration is to reproduce with adequate statistic in the controlled environment of the laboratory the γ -ray interactions under space conditions. The total number of required incident γ -rays N_T , not necessarily interacting within the GRID, depends on the expected counting statistics for bright astrophysical sources acquired for typical exposures. With the goal of achieving statistical errors due to the calibration negligible compared to those in flight, we require a number of events about four times larger than the brightest source.

The canonical source of in-flight calibration is the Crab Nebula with an integrated average total γ -ray flux (nebula and pulsar) of $I_c(E_\gamma > 100 \text{ MeV}) = 220 \times 10^{-8} \text{ ph/cm}^2/\text{s}$ (Pittori et al. 2009) and the calibration statistics is estimated based on its flux and the AGILE detection capability (Tavani et al. 2009). The Crab Nebula integral γ -ray intensity flux as a function of the γ -ray energy E_γ expressed in MeV is $I_c(E_\gamma > 100 \text{ MeV}) = E_\gamma^{-1.015} 2.36 \times 10^{-4} \text{ ph/cm}^2/\text{s}$.

For a given incident direction (Θ, Φ) , the number of required incident γ -rays with $E_\gamma > E_{\text{th}}$ is $N(E_{\text{th}}, \Theta, \Phi) = \alpha t_{\text{exp}} \eta A_{\text{geom}} I_c(E_\gamma)$, where $\alpha = 4$ is the factor required to reduce to negligible levels the statistical error due to calibration, η is the Earth occultation efficiency (typically $\eta = 0.45$), t_{exp} the exposure time (typically $t_{\text{exp}} = 2$ weeks) and A_{geom} the geometric area of the GRID ($A_{\text{geom}} = 1600 \text{ cm}^2$).

For typical values and the GRID geometry, we obtain the integrated required number of incident γ -ray for $E_\gamma > 30 \text{ MeV}$ for a given combination of (Θ, Φ) :

$$N(30 \text{ MeV}, \Theta, \Phi) = 2.6 \times 10^4 \text{ ph.} \quad (7)$$

3.3. Calibration set up

The tagged γ -ray beam used for the calibration has been already described in detail in Cattaneo et al. 2012. In the following the most relevant elements are briefly summarised.

3.3.1. The Beam Test Facility

For the GRID calibration we used the Beam Test Facility (BTF) in the Frascati DAΦNE collider complex, which includes a LINAC at high electron and positron currents, an accumulator of $e^+ - e^-$ and two accumulation rings at 510 MeV. The e^+/e^- beam from the LINAC is led into the accumulation ring to be subsequently extract and injected in the Principal Ring. When the system injector does not transfer the beams to the accumulator, the beam from LINAC can be transported in the test beam area through a dedicated transfer line: the BTF line (Fig. 2). The BTF can provide a collimated beam of electrons or positrons in the energy range 20 MeV to 800 MeV with a pulse rate of 49 Hz. The pulse duration can vary from 1 ns to 10 ns and the average number of particles for bunch from 1 to 10^{10} . In Fig. 2 a schematic view of the calibration set up is shown.

The BTF can be operated in two ways

- a LINAC mode operating when DAΦNE is off with a tunable energy in the range 50 MeV to 750 MeV and an efficiency around 0.9
- a DAΦNE mode operating when DAΦNE is on with a fixed energy of 510 MeV and an efficiency around 0.6

3.3.2. Target

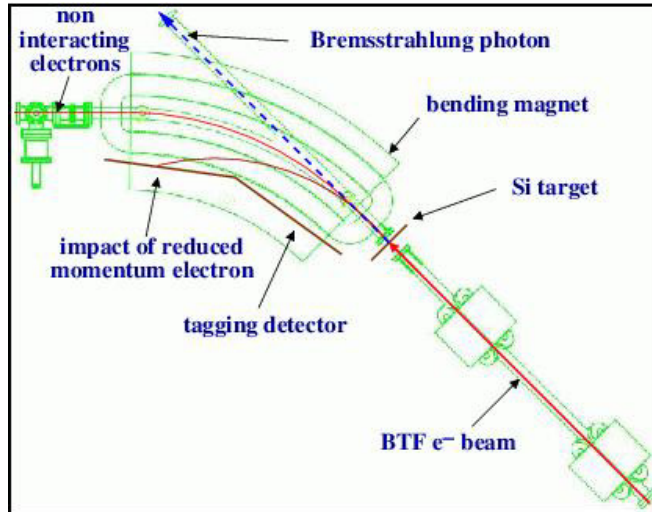


Figure 2. Schematic view of the γ -ray line: the target, the spectrometer magnet and the Photon Tagging System (PTS).

Beam electrons cross perpendicularly the thin silicon microstrip detectors acting as target, producing γ -rays in the energy range of interest to the GRID by Bremsstrahlung; subsequently a dipole magnet bends away electrons while γ -rays follow straight trajectories and can reach the GRID instrument.

The target consists of two pairs of single-sided silicon microstrip detectors 0.41 mm thick of area $8.75 \times 8.75 \text{ cm}^2$. Each detector includes 384 strips with $228 \mu\text{m}$ pitch. The target has two functions: measuring the passage of each electron and causing the emission of Bremsstrahlung γ -rays.

3.3.3. Photon Tagging System (PTS)

Our team developed and installed in the BTF area a Photon Tagging System (PTS) for the detection of the electrons that produce Bremsstrahlung γ -rays in the target (Cattaneo et al. 2012). In absence of significant energy loss due to Bremsstrahlung, the electrons follow a circular trajectory inside a guide inserted in the dipole magnet without interacting, as sketched in Fig. 2. The internal wall of the guide is covered by silicon microstrip detectors; therefore, in presence of emission of Bremsstrahlung γ -rays of sufficient energy, the electrons follow a more curved trajectory and hit one of the microstrip detectors in a position correlated to the energy loss. After calibrating with MC simulation the relation between PTS hit position and γ -ray energy, the PTS position measurement provides an estimator of the γ -ray energy E_{PTS} .

3.3.4. Trade-off on the number of e^- /bunch

The overall GRID performance should be tested in a single-photon regime without simultaneous multi-photon interactions, which are not represent astrophysical conditions and cannot be easily identified during the calibration. Multi-photon interactions represent an intrinsic noise that may bias significantly the measure of the A_{eff} and of the EDP.

Ideally, one γ -ray should be emitted by one electron crossing the target, but both the actual number of electrons in each bunch and the number of emitted Bremsstrahlung γ -rays are stochastic variables. Therefore multi-photon emission cannot be eliminated completely.

For the calibration a compromise between BTF efficiency and calibration accuracy had to be found. In the DAΦNE mode with 5 e^- /bunch the fraction of events with multiple γ -rays having $E_\gamma > 20$ MeV is $\sim 5\%$. This uncertainty is comparable to the accuracy requirement on the measurement of A_{eff} . On the other hand, the DAΦNE mode with 1 e^- /bunch is consistent with an accuracy requirements $\sim 1\%$ but reduces the number of configurations/directions that can be calibrated due to the constraint of available time.

Taking into account the above considerations, the configuration with 3 e^- /bunch was chosen as compromise between reduced multi-photon events and sufficient statistics.

3.3.5. Mechanical Ground Support Equipment

Our team developed and installed in the BTF area a Mechanical Ground Support Equipment (MGSE) that was used for the AGILE calibration (Gianotti et al. 2008). The MGSE permitted the rotation and translation of AGILE relatively to the beam. A rotation is parametrised by the polar angle Θ and azimuthal angle Φ of the beam direction with respect to the AGILE coordinate system. Using the translation capability of the MGSE, for each run the beam was focused in a predefined position on the GRID.

3.3.6. Simulation

The overall system, including the beam terminal section, the target, the bending magnet, the PTS and the GRID is simulated in detail using GEANT 3.21 package (Cocco et al. 2001, 2002). This allows a direct comparison between the resolutions measured in simulated and real data providing a validation of the MC simulations. An improvement of the comparison between data and MC is obtained by overlapping a uniform flux of low energy photons to the Bremsstrahlung γ -ray. These photons are beam related and are a background that cannot be precisely estimated and is tuned to match the experimental data.

4. DATA SAMPLES

During the calibration campaign $\sim 2.7 \times 10^6$ PTS events were detected, of which $\sim 40\%$ have interacted with the GRID; they impinged in different positions on the GRID for a set of predefined incident directions. Polar angles Θ between 0° and 65° and azimuthal angles Φ between 0° and 315° were tested. Table 1 presents a detailed account of the data samples versus the beam incident angles. For each direction, the number of PTS events is significantly larger, and also the number of tagged γ -rays is at least comparable, than the number in Eq. 7 guaranteeing small statistical errors.

For each direction, a set of incident positions was selected to provide an approximate coverage of the detector area; some examples are shown in Fig. 3. It is nevertheless evident that the coverage is very approximate with the partial exception of the configuration $\Theta=0^\circ$, $\Phi=0^\circ$. This makes impossible a direct estimation of the A_{eff} that requires a uniform illumination of the instrument.

5. ANALYSIS OF EVENTS

5.1. The GRID Trigger

A great challenge in γ -ray astronomy is due to the fact that cosmic rays and the secondary particles produced by the interaction of cosmic rays in the atmosphere produce in detectors a background signal much larger than that produced by cosmic γ -rays. Therefore the development and the optimisation of the trigger algorithms to reject this background have been of primary relevance for AGILE. AGILE have a Data Handling system (Argan et al. 2008; Tavani et al. 2008) which cuts a large part of the background rate through a trigger system, consisting of both hardware and software levels, in order not to saturate the telemetry channel for scientific data.

The on-board GRID trigger is divided into three levels: two hardware (Level 1 and 1.5) and one software (Level 2) (Giuliani et al. 2006). The hardware levels accept only the events that produce some particular configuration of fired anticoincidence panels and ST planes. The main goal of the two hardware trigger levels is to select γ -rays and provide a rejection factor of ~ 100 for background events. The software level provides an additional rejection of the background by a factor ~ 5 .

The residual background events are further reduced offline on ground by more complex software processing. In the first step software algorithms are applied that analyse the event morphology, based on cluster identification and

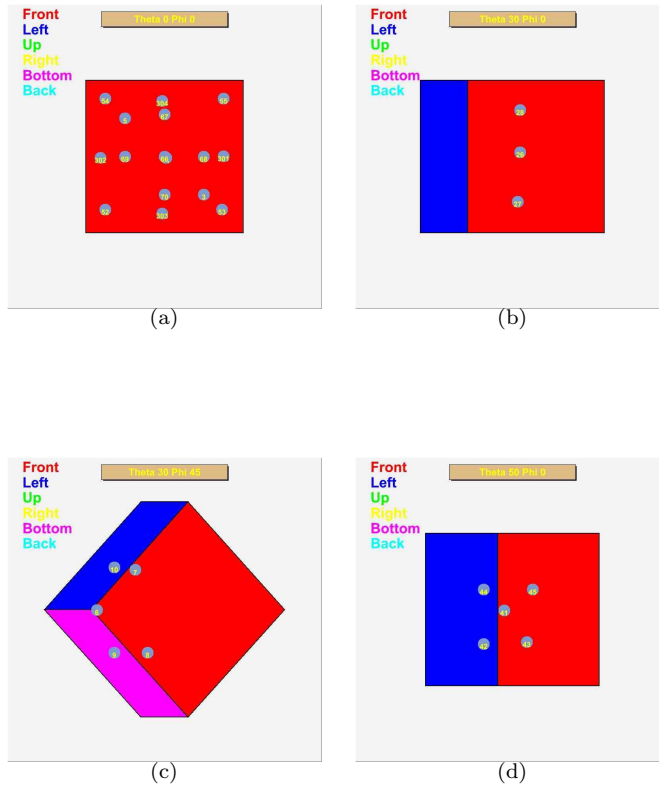


Figure 3. Beam incident positions for a) $\Theta=0^\circ, \Phi=0^\circ$ b) $\Theta=30^\circ, \Phi=0^\circ$, c) $\Theta=30^\circ, \Phi=45^\circ$, d) $\Theta=50^\circ, \Phi=0^\circ$.

topology to reduce the background. A further processing step is necessary to eliminate the remaining background events, particularly those produced by albedo γ -rays which are discriminated by cosmic γ -rays only on the basis of their incoming direction. (see [Vercellone et al. 2008](#) for a description of the AGILE on-ground data reduction).

5.2. The PTS trigger

The trigger for reading out the target and the PTS data was delivered by the accelerator and was independent from the PTS data themselves. Therefore the PTS events were triggered independently from the GRID and written on a separate stream. Further selection based on the PTS data was performed offline by requiring that one or more strip clusters were identified. A cluster was defined as a set of neighbouring strips on the same detector above a predefined threshold. The signal over noise was high enough that the algorithm selected essentially all electrons crossing the detector ([Cattaneo et al. 2012](#)).

5.3. Event selection for data

The PTS events and the GRID ones, which are written on two different streams, are correlated offline exploiting the time tags recorded for both event streams. The result is a subset of GRID events that can be associated, for each event, to the γ -ray energy estimated by the PTS E_{PTS} . The fraction of events with a PTS trigger and without a GRID trigger provides an estimation of the efficiency of the GRID.

5.4. Event selection for MC

MC sets are simulated reproducing precisely the beam parameters and the position and orientation of the GRID with respect to the beam as well as online and offline trigger conditions. Event samples comparable in size to the data are generated. The events are selected by requiring that the trigger conditions are satisfied by PTS and GRID signals, so that direct comparison with data is possible.

Table 1. Size of data samples taken in various configurations: in the first two columns the polar and azimuthal angles of the AGILE axis with respect to the beam, in the third the number of events with a GRID trigger, in the fourth the number of events with a PTS trigger, in the fifth the number of events with the GRID-PTS triggers in time, in the sixth the ratio between the fifth and the fourth columns, representing, approximately, the GRID efficiency.

Θ	Φ	GRID events	PTS events	Tagged γ	$\epsilon(\%)$
0°	0°	584873	682269	284726	41.7
30°	0°	107132	133322	59751	44.8
30°	45°	332604	458633	192872	42.1
30°	135°	290792	379584	157908	41.6
30°	225°	154379	176824	70898	40.1
30°	270°	155636	180578	84477	46.8
30°	315°	63367	75048	33811	45.0
30°	all	1103910	1403989	599797	42.7
50°	0°	219479	227402	108656	47.8
50°	270°	127389	135887	66647	49.0
50°	315°	164296	183198	85351	46.6
50°	all	511164	546487	260654	47.7
65°	0°	49745	46369	22799	49.2
65°	315°	51359	40759	21509	52.8
65°	all	101104	87128	44308	50.8
all	all	2301051	2719873	1189485	43.7

5.5. PTS as energy estimator

The rationale behind the use of E_{PTS} as energy estimator in measuring the GRID resolutions is the expectation that the resolution of E_{PTS} is much better than that of E_{GRID} . That can be verified for MC events of class G comparing the distributions of E_{PTS} versus E_γ as well as E_{GRID} versus E_γ and verifying that the former distribution is much narrower than the latter. Those distributions are shown in Fig.4a and Fig.4b, respectively, with the red markers representing the average E_{PTS} in E_γ bins 50 MeV wide. It is apparent that the resolution of E_{PTS} as an energy estimator of E_γ is much better than that of E_{GRID} and therefore E_{PTS} provides an effective energy estimator for calibrating the GRID with real data under the mild assumption that the energy resolution of E_{PTS} for data is not much worse than that for MC.

6. RESULTS

As shown in Table 1, data have been collected for different values of Θ and Φ . In principle all figures of merit presented in Sect. 3.1 depend on Θ and Φ but within the statistics collected no dependence on Φ is visible. Therefore, in the following, the data collected for different values of Φ and the same value of Θ are grouped together, and the results are presented as dependent on Θ only.

6.1. Energy Dispersion Probability from real and MC data

The EDP defined in Eq.4 can be obtained illuminating uniformly the GRID with a monochromatic beam of γ -rays with energy E_γ and considering the resulting spectrum of E_{GRID} . This procedure, repeated for an adequate number of energies E_γ , allows to build a matrix (E_γ, E_{GRID}) defining the EDP. This can be done with MC simulations but, not being available monochromatic γ -ray beams of variable and known energy with sufficient size to guarantee uniform illumination, cannot be done experimentally.

In any case, this approach is not the most appropriate for the application to which GRID is dedicated. The γ -ray spectra measured by GRID during its operation in flight are power-law spectra like $1/E_\gamma^\alpha$ with $\alpha \sim 1.7$ (Chen et al. 2013), therefore a matrix is built with MC events produced according to this power-law spectrum $(E_\gamma, E_{GRID})_{1.7}^{MC}$ (the subscript is the power index).

The goal of the BTF calibration is to assess quantitatively the reliability of the MC simulation used to build the EDP matrix, not to measure the EDP matrix directly. One reason is that the BTF γ -ray beam follows an approximate

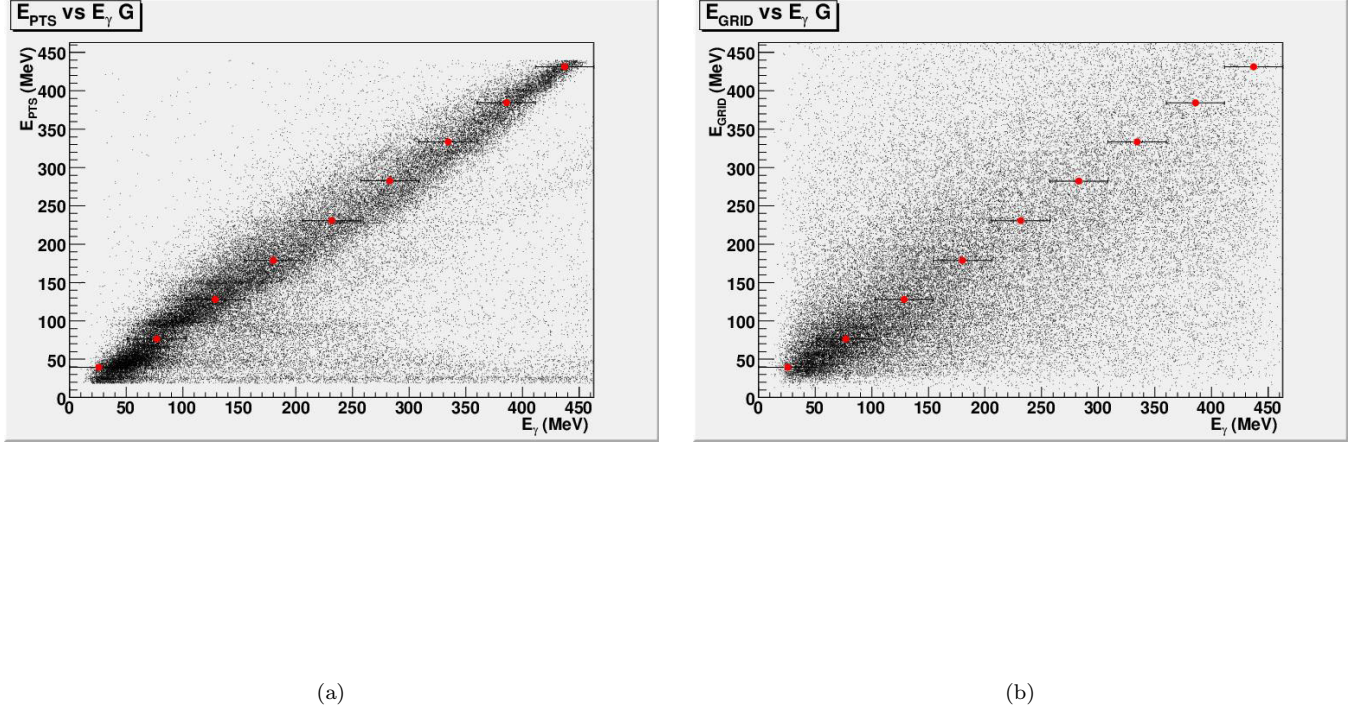


Figure 4. MC events of class G: a) Relation between E_{PTS} and E_γ ; b) Relation between E_{GRID} and E_γ . The red circles are the average E_{PTS} in the true energy E_γ bin.

$1/E_\gamma$ Bremsstrahlung spectrum on the restricted energy range available producing an EDP matrix different from the one estimated using a power-law spectrum whose spectral index is $\alpha = 1.7$ (Chen et al. 2013); the other reason is that the true energy E_γ of the single γ -ray is unknown. At the BTF, a straightforward comparison is possible between $(E_{PTS}, E_{GRID})_{1.0}^{data}$ and $(E_{PTS}, E_{GRID})_{1.0}^{MC}$. Our goal is to estimate the effect of the discrepancies measured in this comparison of the errors between $(E_\gamma, E_{GRID})_{1.7}^{data}$ and $(E_\gamma, E_{GRID})_{1.7}^{MC}$, that are the actual systematic errors in the EDP.

In Fig.5 the events are partitioned in five E_{PTS} bins and the distributions of E_{GRID} are displayed for MC (blue) and real data (red). The variable $\log(E_{GRID})$ is fitted with a Gaussian separately for MC and data in each E_{PTS} bin. The fitted averages and the relative standard deviations are reported in the legend as $\langle E_{GRID} \rangle$ and $\Delta E_{GRID}/\langle E_{GRID} \rangle$.

The values of $\langle E_{GRID} \rangle$ for each energy bin are within or close to the E_{PTS} bins both for MC and real data with the exception of Fig.5a, where, as visible in Fig. 4a, there is in the low energy E_{PTS} bin a significant tail due to high E_{GRID} events. The widths of the distributions for MC and data are well compatible with each other within 5%, that can be assumed as an upper limit estimation of the systematic error, with some discrepancy in Fig.5e for $E_{PTS} \approx 400$ MeV, and consistent with the value estimated in Sect. 2.3.2. The discrepancy in Fig.5e may be due to the poor reliability of E_{PTS} as estimator of E_γ at this energy, as explained in Sect. 5.5.

Similar results are obtained for different values of Θ .

6.2. PSF from real and MC data

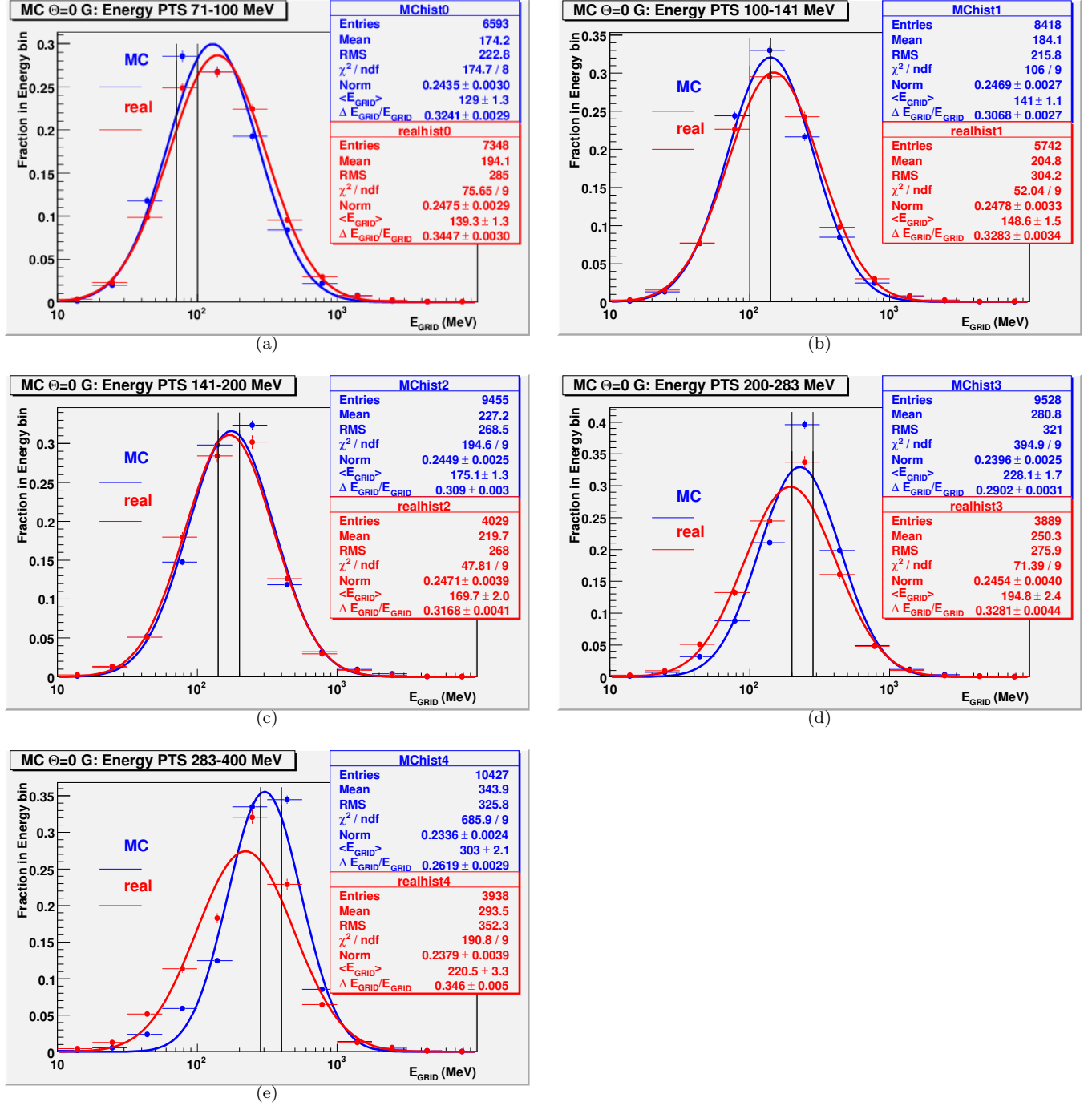


Figure 5. Energy Dispersion Probability for MC (blue) and real data (red) in five bins of E_{PTS} for events of class G and $\Theta=0^\circ$ for a) $71 \text{ MeV} \leq E_{PTS} \leq 100 \text{ MeV}$ b) $100 \text{ MeV} \leq E_{PTS} \leq 141 \text{ MeV}$ c) $141 \text{ MeV} \leq E_{PTS} \leq 200 \text{ MeV}$ d) $200 \text{ MeV} \leq E_{PTS} \leq 283 \text{ MeV}$ e) $283 \text{ MeV} \leq E_{PTS} \leq 400 \text{ MeV}$. The pair of vertical lines delimit the E_{PTS} range used to produce each histograms. See text for more detail.

The performance of the instrument with respect to the angular resolution is characterised by the Point Spread Function (PSF) as defined in Sect.1. The distribution of the three-dimensional angular difference is fitted assuming that the PSF is described by the two parameters King's function as defined in the Appendix. In addition to the function parameters, δ related to the standard deviation and γ related to non-Gaussian tail, also the value of the

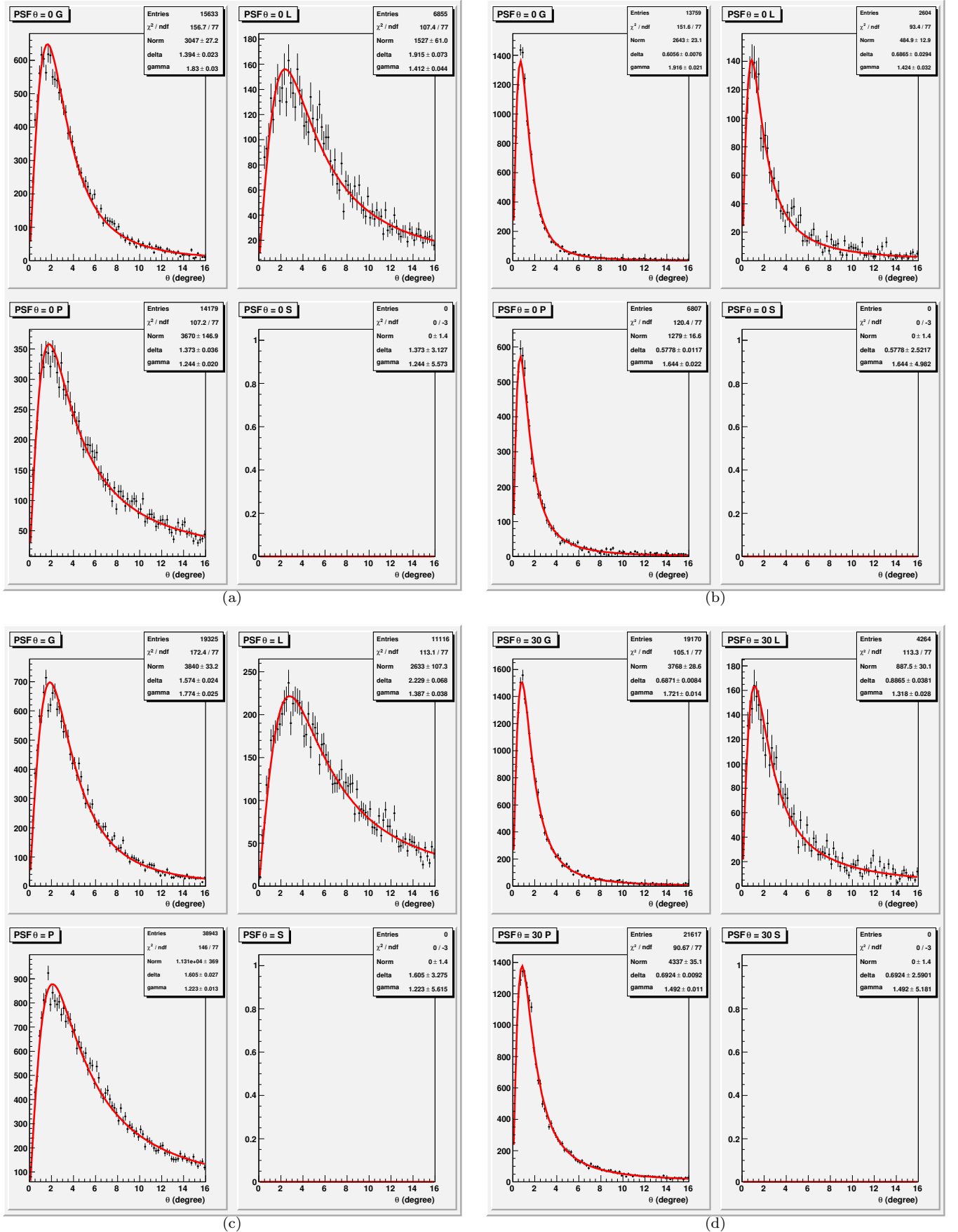


Figure 6. Distributions of the three-dimensional angular difference for MC events with the PSF fitted with King function (the four plots in each quadrant corresponds to events of class G,L,P and S respectively) for a) $\Theta=0^\circ$, $70 \text{ MeV} \leq E_{GRID} \leq 140 \text{ MeV}$ b) $\Theta=0^\circ$, $280 \text{ MeV} \leq E_{GRID} \leq 420 \text{ MeV}$ c) $\Theta=30^\circ$, $70 \text{ MeV} \leq E_{GRID} \leq 140 \text{ MeV}$ d) $\Theta=30^\circ$, $280 \text{ MeV} \leq E_{GRID} \leq 420 \text{ MeV}$.

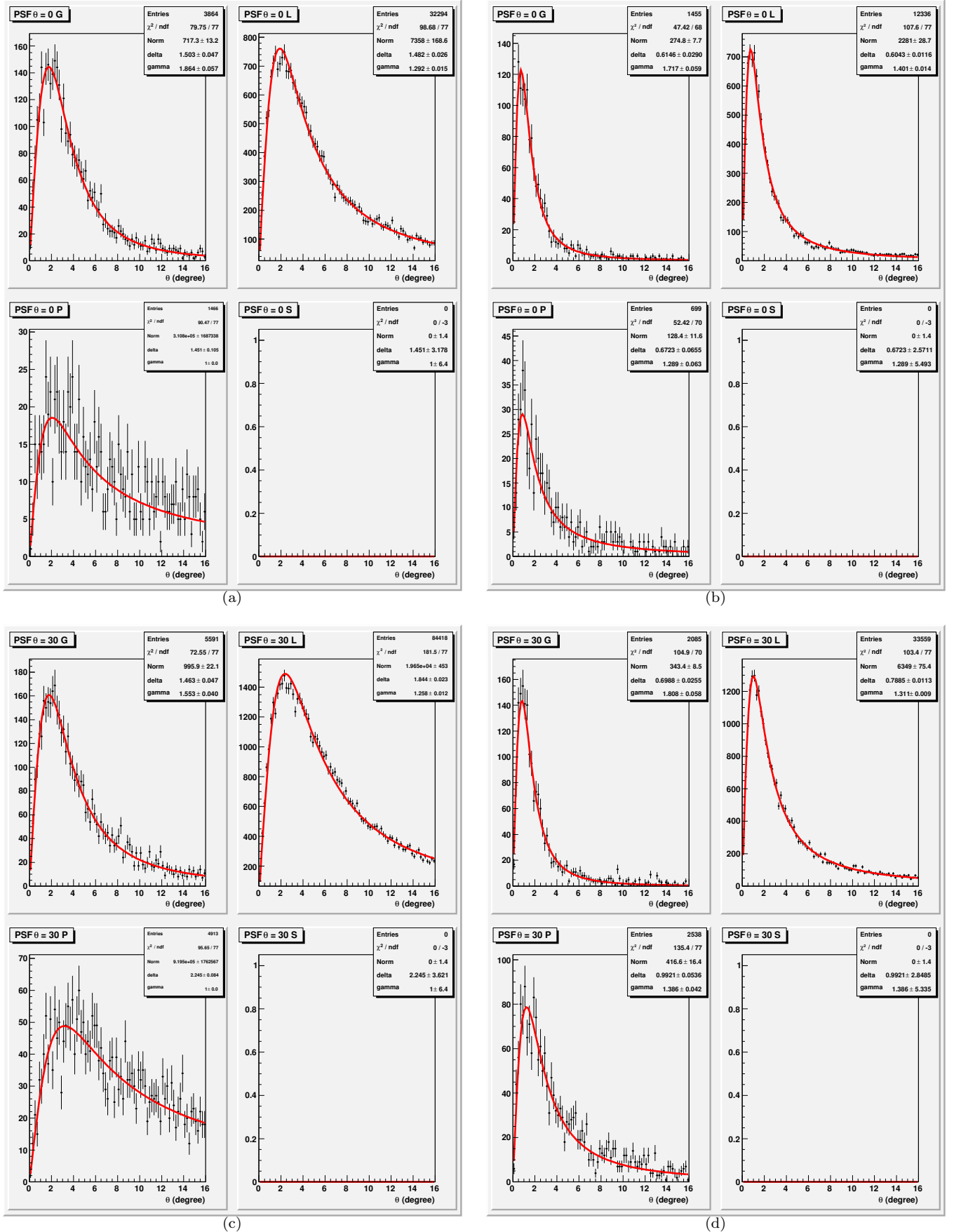


Figure 7. Distributions of the three-dimensional angular difference for real events with the PSF fitted with King function (the four plots in each quadrant corresponds to events of class G,L,P and S respectively) for a) $\Theta=0^\circ$, $70 \text{ MeV} \leq E_{\text{GRID}} \leq 140 \text{ MeV}$ b) $\Theta=0^\circ$, $280 \text{ MeV} \leq E_{\text{GRID}} \leq 420 \text{ MeV}$ c) $\Theta=30^\circ$, $70 \text{ MeV} \leq E_{\text{GRID}} \leq 140 \text{ MeV}$ d) $\Theta=30^\circ$, $280 \text{ MeV} \leq E_{\text{GRID}} \leq 420 \text{ MeV}$.

Table 2. King's function fit parameters of the PSF with the Containment Radius at 68.3% for four energy bins and three angular direction for MC and real data.

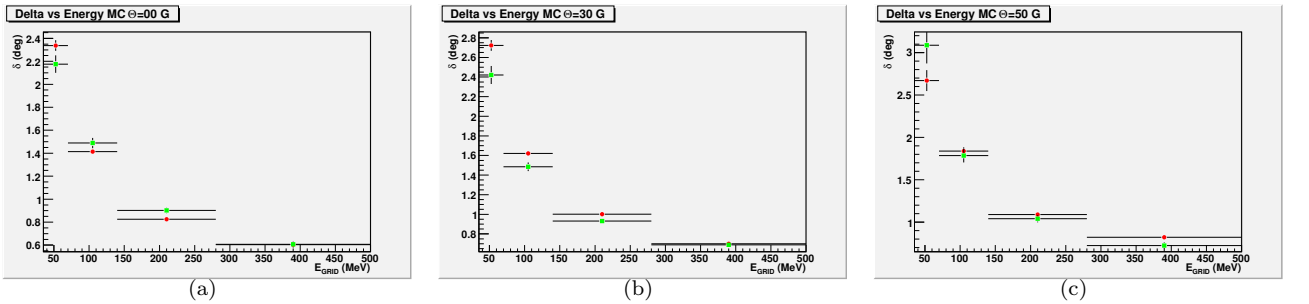
Θ (deg)	E_{PTS} (MeV)	MC			Real		
		δ (deg)	γ	CR_{68} (deg)	δ (deg)	γ	CR_{68} (deg)
0	35-70	2.33±0.05	1.97± 0.03	6.95± 0.17	2.17± 0.08	1.60± 0.04	9.18± 0.36
	70-140	1.41±0.02	1.86± 0.02	4.52± 0.10	1.49± 0.04	1.84± 0.05	4.85± 0.22
	140-180	0.83±0.01	1.87± 0.02	2.61± 0.06	0.90± 0.03	1.92± 0.05	2.77± 0.16
	280-500	0.60±0.01	1.91± 0.02	1.87± 0.06	0.61± 0.03	1.69± 0.06	2.27± 0.23
30	35-70	2.72±0.05	2.03± 0.04	7.77± 0.19	2.42± 0.09	1.45± 0.03	14.15± 0.57
	70-140	1.62±0.02	1.85± 0.02	5.25± 0.10	1.48± 0.04	1.58± 0.03	6.54± 0.25
	140-180	1.00±0.01	1.82± 0.01	3.29± 0.06	0.93± 0.03	1.70± 0.04	3.47± 0.16
	280-500	0.70±0.01	1.76± 0.01	2.45± 0.05	0.69± 0.03	1.77± 0.05	2.38± 0.22
50	35-70	2.67±0.12	1.76± 0.08	9.36± 0.17	3.09± 0.22	1.41± 0.07	19.83± 1.47
	70-140	1.84±0.06	1.88± 0.04	5.86± 0.10	1.78± 0.06	1.58± 0.06	7.89± 0.44
	140-180	1.05±0.02	1.76± 0.02	3.86± 0.06	1.04± 0.04	1.60± 0.04	4.40± 0.26
	280-500	0.82±0.02	1.66± 0.02	3.26± 0.06	0.73± 0.06	1.48± 0.05	3.93± 0.35

Containment Radius at 68.3% (CR_{68}) is quoted: this value is determined by the function parameters, but it can be defined independently from the parametrisation.

The angular distributions are fitted separately for different incident angles (Θ), different classes (G,L,S,P) and different intervals of energy. A subset of these fits is shown in Fig.6 for MC events and in Fig.7 for real events for two bins of E_{GRID} for $\Theta = 0^\circ$ and $\Theta = 30^\circ$. The quality of all fits is good both for MC and real data. In Fig.8-9-10 the results of the King's function parameters obtained with the fits for MC and real data are shown versus E_{GRID} . In general the comparison is satisfying, although the parameter γ for data is significantly lower than for MC especially for low E_{GRID} . This implies larger Containment Radius boundaries for data at low energy.

Considering the broad EDP, especially at low energy, it is worth investigating if the choice of the energy estimator influences significantly the PSF parameters. E_{GRID} and E_{PTS} are available for both data and MC while only E_γ is available for MC events. In Fig.11-12, the parameters of the King's function from MC and real data are displayed versus the relevant energy estimators. The agreement is good, the King's parameters for the same energy bin rarely differs more than 2-3 σ , with the exception of the last E_{PTS} bin in real data, where the environmental background induces a large fraction of PSF events unrelated to real γ -rays of corresponding energy in the GRID as discussed in Sect. 5.5.

In Table 2 the results of the fits of the PSF distributions with the King's function are reported versus the γ -ray energy for three incident angles for MC and real data. The agreement is quite satisfactory with the exception of the parameter γ and consequently CR_{68} for the lowest energy channel where real data PSFs show consistently longer tails.


Figure 8. Parameter δ of the King's function versus measured γ -ray energy E_{GRID} for real (green squares) and MC (red circles) events: a) $\Theta=0^\circ$, b) $\Theta=30^\circ$, c) $\Theta=50^\circ$

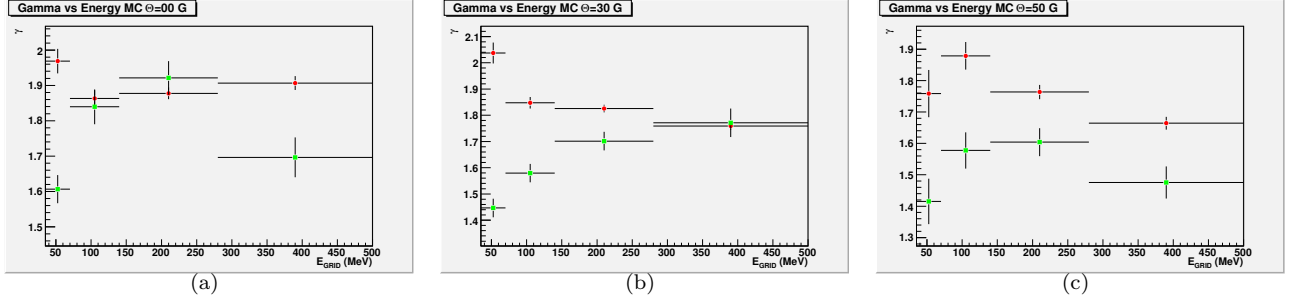


Figure 9. Parameter γ of the King's function measured versus γ -ray energy E_{GRID} for real (green squares) and MC (red circles) events a) $\Theta = 0^\circ$, b) $\Theta = 30^\circ$, c) $\Theta = 50^\circ$

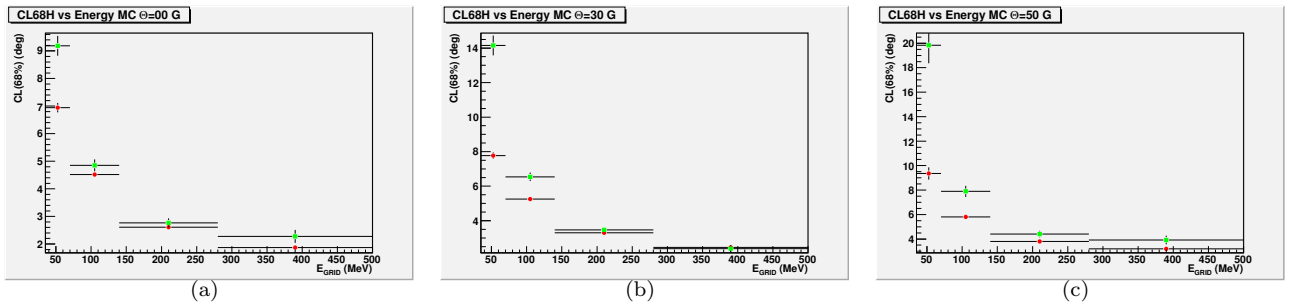


Figure 10. Containment Radius 68.3% of the King's function versus measured γ -ray energy E_{GRID} for real (green squares) and MC (red circles) events a) $\Theta = 0^\circ$, b) $\Theta = 30^\circ$, c) $\Theta = 50^\circ$

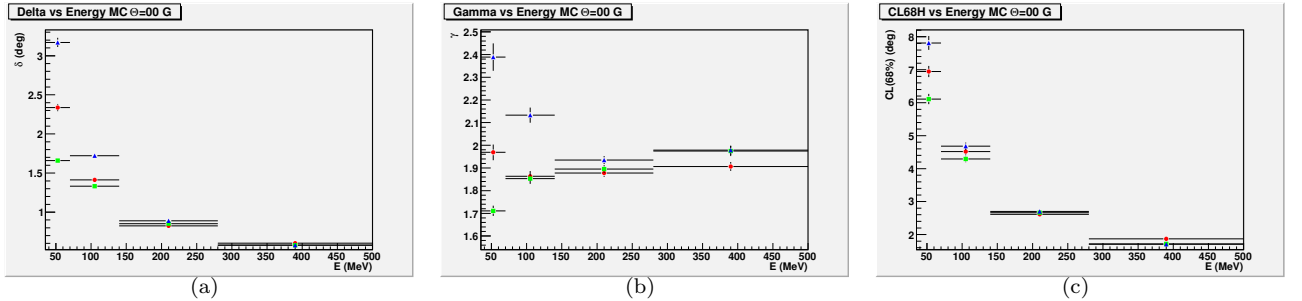


Figure 11. Parameters of the King's function for MC data at $\Theta=0^\circ$ versus different γ -ray energy estimator: E_{GRID} (red circles), E_{PTS} (green squares), E_γ (blue triangles). a) Parameter δ b) Parameter γ , c) PSF Containment Radius $CR_{68\%}$.

6.3. Effective area A_{eff}

This measurement turned out to be the most critical and we are unable to provide significant results. The reason is the strong flux of low energy photons in the experimental hall and, at a smaller extent, cosmic rays. This has been detected and discussed in depth in Cattaneo et al. 2012, that shows that many GRID triggers are fired outside the phase of the beam and some parts of the E_{PTS} spectrum are unrelated to the γ -ray emission due to Bremsstrahlung. Furthermore even for events in phase, there are more hits on the front faces in real data than in MC.

The GRID detection efficiency is expected to be measured by the ratio of GRID events to PTS events in data and MC. The comparison can provide an estimation of the quality of the simulation and eventually provide correction

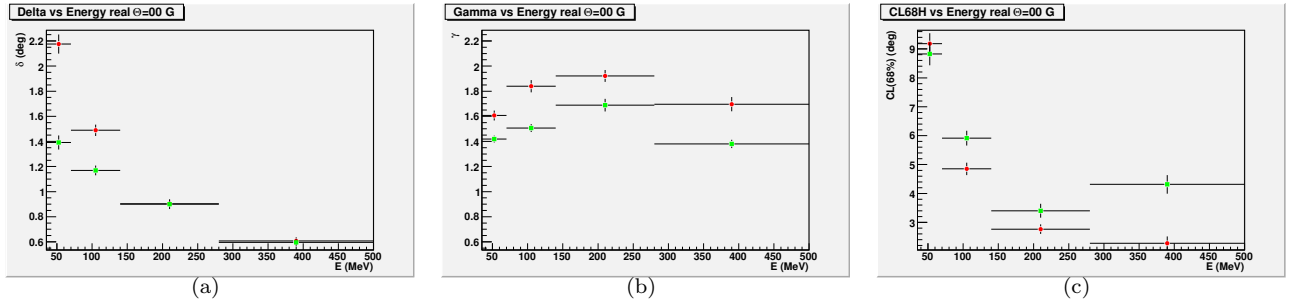


Figure 12. Parameters of the King's function for real data at $\Theta = 0^\circ$ for different γ -ray energy estimator: E_{GRID} (red circles), E_{PTS} (green squares). a) δ b) γ , c) $CR_{68}\%$.

factors. This approach is sensible if the MC reproduces correctly the data and if the calibration data resembles closely those expected in the space configuration. The presence of a significant flux of cosmic rays triggering both the GRID and the PTS at random times are extremely difficult to simulate appropriately and outside the scope of the calibration task.

An additional and even more relevant problem is the flux of low-energy photons in the experimental hall in phase with the beam. The low-energy photons down to X-ray energy are relevant because, if interacting with the silicon detectors, they release enough energy to be above threshold for hit detection. Those photons can be due to photon production along the beam line entering the hall, photon production in the last bending magnet, photon production in the beam dump of the electron beam followed by scattering inside the hall. This part is underestimated in the MC because it would require a simulation of the full hall for such low-energy photons that is unrealistic. Such low-energy photon induced hits can overlap with γ -ray conversion events forcing the filter to move e.g. an event from class G (clean conversion) to class L (ambiguous).

This effect is clearly visible in comparing MC (Fig. 6) and real data (Fig. 7) where the ratio between the numbers of G and L events is completely different being much lower for real data. Additional efforts could bring the MC data closer to real data adding e.g. an additional flux of low-energy photons hitting the GRID but it would be arbitrary and in any case significantly different from the space configuration so that little or no information would be harvested.

Nevertheless this discrepancy is much less relevant for the measurements of the PSF and EDP for class G events because for those measurements we rely on events already classified as class G, that is for events for which the influence of the low-energy photons is non-existent or negligible. Under those conditions, the comparison between MC and real data is realistic and the calibration results is expected to reproduce those in the space configuration.

7. CONCLUSIONS

In this paper the results of the calibration of the AGILE tracker GRID in the range 35 MeV to 450 MeV on the BTF beam are presented. In particular the EDPs and the PSFs versus the γ -ray energy and the incident angle have been measured and compared with the MC expectations with satisfactory results, while a reliable estimation of A_{eff} turned out to be unfeasible. From this comparison we quantify the reliability of the MC in describing the data and therefore in estimating the systematic errors associated to the EDP matrices and PSF functions built with the MC and used in the analysis of in-flight AGILE data. The differences in average values and in widths of the real and MC EDPs are mostly within 5% as shown in Fig.5 (except for the highest energy). The differences in PSFs mostly within 2-3 σ with a few exceptions .

These results qualify AGILE as an instrument particularly effective in performing accurate measurements in the γ -ray energy range 50 MeV to 450 MeV as confirmed by in-flight observations (Sabatini et al. 2015).

APPENDIX

The PSF of instruments measuring high energy γ -rays is best characterised by the King's function $k(\theta)$ (King 1962; Chen et al. 2013). The King's function can be defined by

$$\begin{aligned} dP(\theta) &= k(\theta) \sin \theta d\theta \\ &= \frac{180}{\pi} \left(1 - \frac{1}{\gamma}\right) \left(1 + \frac{(\theta/\delta)^2}{2\gamma}\right)^{-\gamma} \frac{\sin \theta}{\delta} d\frac{\theta}{\delta} \end{aligned} \quad (8)$$

where θ is the three-dimensional angular distance between the nominal and measured values and $dP(\theta)$ is the probability of the angular distance to be between θ and $\theta + d\theta$. The choice of the normalization factor is such that, under the approximation $\frac{180}{\pi} \sin \theta \approx \theta$, where θ is expressed in radian on the left side and in degree on the right one, we obtain

$$P(\theta) = \int_0^\theta k(\theta') \sin \theta' d\theta' = 1 - \frac{1}{\left(1 + \frac{(\theta/\delta)^2}{2\gamma}\right)^{\gamma-1}}$$

$$P(+\infty) = 1 \tag{9}$$

The standard deviation of the King's function is $\sigma = \delta \sqrt{\frac{\gamma}{\gamma-3/2}}$; for $\gamma \rightarrow +\infty$ it converges to a Gaussian and $\sigma \rightarrow \delta$. It is convenient to express the width of the angular PSF in terms of Containment Radius at 68.3% (CR_{68}), that is the angular value for which a predefined fraction of events (68.3% in analogy with the fraction of events falling within a standard deviation for the Gaussian function) falls within the nominal direction. If the PSF is parametrised by a King function, an approximate analytic calculation of the CR_{68} is possible. In order to determine the value CR such that $P(CR) = f$ ($0 \leq f \leq 1$), the function in Eq. 9 can be inverted as

$$CR_f = P^{-1}(f) = \delta \sqrt{2\gamma \left(\frac{1}{(1-f)^{\frac{1}{\gamma-1}}} - 1 \right)} \tag{10}$$

For $\gamma \rightarrow +\infty$, The King's function becomes a Gaussian and Eq.10 becomes

$$CR_f = \lim_{\gamma \rightarrow \infty} \delta \sqrt{2\gamma \left(\exp^{\frac{1}{\gamma-1} \ln \frac{1}{(1-f)}} - 1 \right)}$$

$$= \lim_{\gamma \rightarrow \infty} \delta \sqrt{\frac{2\gamma}{\gamma-1} \ln \frac{1}{(1-f)}}$$

$$= \delta \sqrt{2 \ln \frac{1}{1-f}} \approx 1.5 \delta \quad \text{for } f = 0.683 \tag{11}$$

This result emphasises the difference between the CR of the PSF and that of the three-dimensional angular distribution. Assuming a Gaussian PSF (and reporting as subscript the percentage rather than the fraction): for the PSF $CR_{68.3} = \delta$, $CR_{95.5} = 2\delta$, $CR_{99.7} = 3\delta$; for the three-dimensional distribution, $CR_{68.3} \approx 1.51 \delta$, $CR_{95.5} \approx 2.49 \delta$, $CR_{99.7} \approx 3.44 \delta$.

ACKNOWLEDGMENTS

The authors would like to thank the staff of the BTF at Laboratori Nazionali di Frascati who made this work possible.

REFERENCES

- Argan, A. et al. 2008, in IEEE Nuclear Science Symposium Conference Record, Dresden, Germany
- Barbiellini, G. et al. 2002, Nucl. Instr. and Meth. A, 490, 146
- Brun, R. et al. 1993, GEANT3-Detector Description and Simulaton Tool, CERN Program Library Long Writeups W5013
- Bulgarelli, A. et al. 2010, Nucl. Instr. and Meth. A, 614, 213
- Cattaneo, P. 1990, Nucl. Instr. and Meth. A, 295, 207
- Cattaneo, P. W. et al. 2012, Nucl. Instr. and Meth. A, 674, 55
- Chen, A. 2012, in Space Telescopes and Instrumentation 2012: Ultraviolet to Gamma Ray, ed. M. J. L. Turner & K. A. Flanagan, Vol. 8443 (SPIE), 8443E
- Chen, A. et al. 2011, GRID Scientific Analysis User Manual, AGILE-IFC-OP-009_Build-21, agile.asdc.asi.it/publicsoftware.html
- Chen, A. et al. 2013, Astron. & Astrophys., 558, A37
- Cocco, V., Longo, F., & Tavani, M. 2001, in American Institute of Physics Conference Series, Vol. 587, Gamma 2001: Gamma-Ray Astrophysics, ed. S. Ritz, N. Gehrels, & C. R. Shrader, 744-748

- Cocco, V., Longo, F., & Tavani, M. 2002, *Nucl. Instr. and Meth. A*, 486, 623
- Feroci, M. et al. 2007, *Nucl. Instr. and Meth. A*, 581, 728
- Früwirth, R. 1987, *Nucl. Instr. and Meth. A*, 262, 444
- Gianotti, F. et al. 2008, in *Space Telescopes and Instrumentation 2008: Ultraviolet to Gamma Ray*, ed. M. J. L. Turner & K. A. Flanagan, Vol. 7011 (SPIE), 70113D
- Giuliani, A. et al. 2006, *Nucl. Instr. and Meth. A*, 568, 692
- Kalman, R. 1960, *Trans. ASME-J. Basic Eng. Ser. D*, 82, 35
- King, I. 1962, *Astron. J.*, 67, 471
- Labanti, C. et al. 2009, *Nucl. Instr. and Meth. A*, 598, 470
- Perotti, F. et al. 2006, *Nucl. Instr. and Meth. A*, 556, 228
- Pittori, C. & Tavani, M. 2002, *Nucl. Instr. and Meth. A*, 488, 295
- Pittori, C. et al. 2009, *Astron. & Astrophys.*, 506, 1563
- Prest, M. et al. 2003, *Nucl. Instr. and Meth. A*, 501, 280
- Sabatini, S. et al. 2015, *Astrophys. J.*, 809, 60
- Tavani, M. et al. 2008, *Nucl. Instr. and Meth. A*, 588, 52
- Tavani, M. et al. 2009, *Astron. & Astrophys.*, 502, 995
- Vercellone, S. et al. 2008, *Astrophys. J. Lett.*, 676, L13